



# Mass transfer from a soluble wall into gas-liquid slug flow in a capillary tube

M.C.F. Silva, J.B.L.M. Campos, J.D.P. Araújo \*

Centro de Estudos de Fenómenos de Transporte, Departamento de Engenharia Química, Faculdade de Engenharia da Universidade do Porto, Rua Dr. Roberto Frias, 4200-465 Porto, Portugal

## ARTICLE INFO

### Article history:

Received 28 August 2018

Received in revised form 26 November 2018

Accepted 4 December 2018

### Keywords:

Mass transfer

Taylor bubble

CFD

VOF

Capillary tube

## ABSTRACT

The mechanism of wall-liquid mass transfer of a solute in micro-scale systems has a huge relevance in many practical scenarios with particular interest for medical devices. A possible enhancement on this kind of phenomenon through the application of slug flow regime was studied with CFD techniques. Different flow conditions were considered to enable the inspection on the distinct hydrodynamics that may occur on the Taylor bubble surroundings in micro-scale. The VOF methodology was used to track the gas-liquid interface and the mass and hydrodynamic fields were simultaneously solved.

The effects of the bubble passage on the mass transfer from a finite soluble wall to the flowing fluid were analyzed for each flow condition, and the corresponding mass transfer coefficients were quantified.

Overall, this numerical work indicates that the flow due to the presence of one Taylor bubble leads to a moderate increase of the wall-liquid mass transfer coefficients. This increase can be enhanced if, instead of one, a continuous flow of bubbles is considered. The abrupt variation on the wall shear stress induced by the bubble movement is important to promote the referred increase.

© 2018 Elsevier Ltd. All rights reserved.

## 1. Introduction

The interest in processes regarding small devices (characteristic dimensions below 1 mm) has emerged in the last decades [1,2]. These small scale processes offer many advantages, being among them the enhancement of heat and mass transfer rates when compared with their macro-scale counterparts [1,3–6], in part due to an increase of the surface area per volume unit. In chemical reactive processes, small devices also allow for a reduction on the amount of reactants needed and an easier scale-up [2]. These advantages and benefits drove to a fast dissemination of their use [1].

Despite the notable advances that have been achieved, manufacturing limitations and the lack of straightforward approaches for creating integrated and flexible systems still offer some obstacles for the use of small devices. Another problem is the susceptibility of this kind of equipment to clogging. Perfect examples are medical micro-devices such as catheters. Due to their unavoidable contact with microorganisms, these can easily adhere to the devices walls and form biofilms which may cause flow blockage [7–9]. In order to control biofilm formation, the wall shear stresses

and the nutrient transport are important factors that should be considered.

According to previous studies performed in macro-scale systems [10,11], the addition of a Taylor bubble to a flowing liquid is able to enhance the mass transfer rates on the wall and, by consequence, can help in controlling the biofilm development. The main purpose of this paper is to investigate the same kind of influence inside a micro-channel. In the future, this knowledge will be essential to define more efficient strategies for biofilm growth control.

The phase distribution occurring on milli/micro-scale gas-liquid flow has been extensively studied. [12–16] As a reference work, Triplett et al. [13] focused on air-water flow inside 1.45 mm circular channels and described five main flow patterns: bubbly, slug, churn, slug-annular and annular.

From these flow patterns, there is a special interest in slug flow. In milli/micro-scales, this pattern persists under a wide range of operating conditions (flow rates as well as different fluids) [13,16] and is characterized by the presence of large bubbles occupying almost all the cross section of the tube (Taylor bubbles). These bubbles are followed by liquid slugs while a liquid film can appear between the bubbles and the channel wall.

The hydrodynamic characteristics involved in Taylor bubbles flow have been analyzed in several numerical and experimental studies, not only in macro-scale systems [17–21], but also in milli

\* Corresponding author.

E-mail address: [daraujo@fe.up.pt](mailto:daraujo@fe.up.pt) (J.D.P. Araújo).



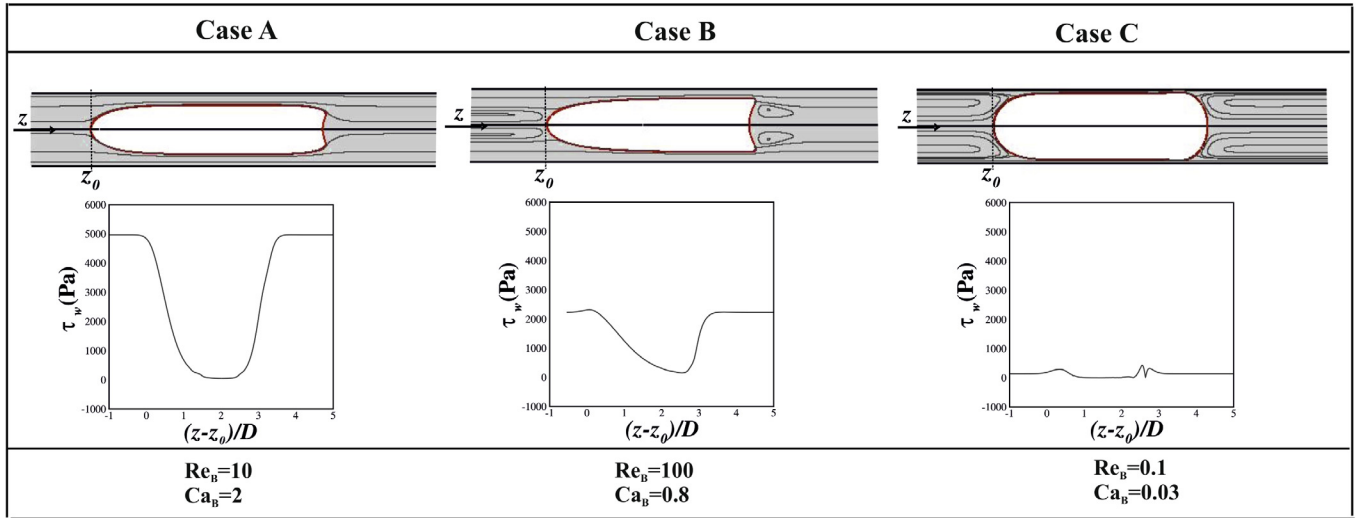


**Fig. 1.** Flow patterns for milli/micro-channels based on the work of Rocha et al. [23]. The wall shear stress axial evolution obtained in the present work is also represented for each flow condition.

- For high Capillary numbers, the bubble moves faster than the liquid ahead of it. The bubble nose is slender, the tail is concave and it is noticeable the existence of a liquid film between the bubble and the wall. In a reference frame moving with the bubble (MRF), there are no recirculation zones in the liquid – Case A.
- For intermediate values of the Capillary number, the bubble still moves faster than the majority of the liquid ahead of it. However, a closed recirculation wake appears below the bubble tail. In a MRF, this wake accompanies the bubble as it moves upwards – Case B.
- Semi-infinite recirculation regions (in MRF) ahead and behind the bubble appear for low values of the Capillary number. As  $Ca_b$  decreases, the cross-sectional area occupied by these recirculation zones gets higher (always increasing from the tube center to the wall). The average velocity of the liquid enclosed in these regions is equal to the bubble velocity, i.e., gas and liquid phases flow like a piston. The bubble tail and nose have a round shape and it occupies practically all the tube cross-section with a very thin liquid film flowing around. This film can be seen as practically stagnant – Case C.

Hatziantoniou and Andersson [28] presented a study where experimental and numerical techniques were used to describe the mass transfer from a soluble wall into a gas-liquid slug flow in milli-channels (diameters between 2 and 3 mm). The authors developed a theoretical and empirical model to extract a correlation for the mass transfer coefficients supported by data produced with different gas and liquid slug lengths, gas and liquid velocities and tube diameters:

$$Sh = 3.51 \left( \frac{ReSc}{L/D} \right)^{0.44} \left( \frac{L_l}{D} \right)^{-0.09} \quad (6)$$

where  $D$  stands for tube diameter,  $L$  is the length of soluble wall and  $L_l$  is the liquid slug length.

The model they developed assumes that no liquid flows around the bubble, and so, gas and liquid are moving in plug flow.

Berčić and Pintar [29] studied the dissolution of benzoic acid in capillaries, assuming also a stagnant liquid film between the flowing bubble and the tube wall. The authors were able to provide experimental data which was correlated using the average gas-liquid slug unit velocity  $u_{us}$ :

$$k_s a = 0.069 u_{us}^{0.63} / ((1 - \varepsilon_G) L_{us} - 0.105 L_{us} \varepsilon_G)^{0.44} \quad (7)$$

where  $L_{us}$  stands for the length of one gas-liquid slug unit, and  $\varepsilon_G$  for the gas hold-up.

van Baten and Krishna [30] studied the mass transfer from a solid wall to a gas-liquid system flowing in circular capillaries using CFD methods. The effects of several hydrodynamic parameters (such as bubble velocity, unit cell length, gas holdup, tube diameter and liquid film thickness) were isolated. The authors characterized the global mass transfer from the wall to the flowing liquid. Afterwards, the soluble wall was separated in two regions: one enclosing the bubble and the other the liquid slug. For each zone, specific Sherwood numbers were calculated. According to the results, for systems with long bubbles (with film lengths higher than  $5D$ ), the values obtained for the Sherwood number in the wall region enclosing the bubble are lower than those for the wall in contact with the liquid slug (assuming that both regions occupy a similar area).

It should be noted that the vast majority of the referred studies, if not all, considered the presence of a stagnant and very thin liquid film between the wall and the bubble. This assumption is a good approximation of the flow behavior described above as case C.

The present work takes advantage of the knowledge about hydrodynamics of two-phase flow in milli/micro-systems, already gathered for a wide range of conditions [23], to study in detail the wall-liquid mass transfer mechanism in slug flow regime. To accurately describe this mechanism, both mass and hydrodynamic fields were solved simultaneously through numerical CFD methods.

This kind of methodologies were already used to study the mass transfer between a soluble wall and a gas-liquid system flowing in a tube with conventional dimensions [11]. In macro-scale, the bubble passage is responsible for an increase on the mass transfer rate. Since the hydrodynamic features differ when the dimension magnitude is considerably reduced, the interest is now placed on evaluating the bubble effect on the mass transfer rates for tubes with smaller diameters. In the future, this knowledge can be transposed to enable an efficient cleaning of organic matter deposited along the wall of capillary tubes.

## 2. Materials and methods

The commercial CFD package ANSYS Fluent 16.2 was used to perform a set of simulations concerning the flow of a single Taylor

bubble through a co-current liquid with simultaneous mass transfer. The effects of the bubble passage on the behavior of mass transfer from a finite soluble wall to the flowing fluid were numerically inspected, and the corresponding mass transfer coefficients were also quantified.

The simulations were performed in a 2D domain by assuming symmetrical conditions along the tube axis. This domain represents half of a cylindrical tube with a diameter of 100  $\mu\text{m}$  and a length equal to 20 diameters. The domain and boundary conditions are illustrated in Fig. 2. The wall of the tube was divided into three main parts: insoluble wall-1, soluble wall-2 and insoluble wall-3. A non-slip condition was applied on these three parts and, regarding the solute transport, the solubility concentration was set at wall-2 and a zero diffusive flux was assumed for walls-1 and 3.

A parabolic velocity profile characteristic of fully developed laminar flow was defined at the capillary inlet. Also at the inlet, a zero solute concentration was imposed. The pressure-outlet condition was set at the tube exit, where a static pressure value is defined. The simulations were performed in transient state to capture the temporal evolution of the solute concentration field.

Regarding the modelling of the system, the continuity (Eq. (8)) and momentum equations (Eq. (9)), already implemented in ANSYS Fluent 16.2, were solved assuming isothermal, incompressible and laminar flow conditions.

$$\frac{\partial}{\partial t}(\rho) + \nabla \cdot (\rho \vec{u}) = 0 \quad (8)$$

$$\frac{\partial}{\partial t}(\rho \vec{u}) + \nabla \cdot (\rho \vec{u} \vec{u}) = -\nabla p + \nabla \cdot (\vec{\tau}) + \vec{F}_\sigma \quad (9)$$

where  $\rho$  represents the density,  $p$  the static pressure,  $\vec{\tau}$  the stress-strain tensor and  $\vec{F}_\sigma$  the interfacial tension force term.

The gas-liquid interface tracking was based on the Volume of Fluid (VOF) method. This method was applied together with the geometric reconstruction scheme that assumes a piecewise-linear approach to describe the interface between phases:

$$\frac{\partial}{\partial t}(\alpha_G) + \vec{u} \cdot \nabla \alpha_G = 0 \quad (10)$$

where  $\alpha_G$  is the gas volume fraction.

The continuum surface model [31] was chosen to translate the effect of the surface tension on the gas-liquid interface:

$$\vec{F}_\sigma = \sigma \omega \frac{\rho \nabla \alpha_G}{0.5(\rho_G + \rho_L)} \quad (11)$$

where  $\omega = -\nabla \cdot \frac{\nabla \alpha_G}{|\nabla \alpha_G|}$ .

Finally, the description of the mass transfer phenomenon involved in this study was based on the “species transport” model implemented in the software. The local mass fraction of each species ( $y_i$ ) was predicted by solving the corresponding mass conservation equation applied to the liquid phase:

$$\frac{\partial}{\partial t}(\rho y_i) + \nabla \cdot (\rho \vec{u} y_i) = -\nabla \cdot \vec{J}_i \quad (12)$$

where  $\vec{J}_i$  represents the diffusive flux of species  $i$ .

The numerical schemes applied to solve the aforementioned set of governing equations followed the choices already taken in previous works [11,32]: (1) PISO (“Pressure-implicit with splitting of operators”) scheme for the solution of the discretized velocity-pressure coupled momentum equations; (2) PRESTO! method was used for the pressure interpolations; (3) QUICK scheme was applied to discretize the momentum equation; and (4) the discretized gradients of the scalars were computed through the “Green-Gauss Node Based” method.

Furthermore, as recommended in the literature [24], the conservative mass equations were solved by an explicit time-marching scheme with a maximum Courant number of 0.25. The time step applied was variable and determined by the Courant number. The convergence criterion assumed in each time step was based on the values of the residuals for momentum and continuity equations that were monitored and controlled to be kept below  $10^{-6}$ .

### 2.1. Mass transfer simulations in the absence of the Taylor bubble

The first step of this work consisted on performing a set of simulations to characterize the mass transfer occurring between a finite soluble wall and a flowing liquid phase. For this purpose, three different liquid viscosities were considered ( $7.5 \times 10^{-3}$ ,  $3.7 \times 10^{-2}$ , and  $4.6 \times 10^{-2} \text{ kg m}^{-1} \text{ s}^{-1}$ ) corresponding to Reynolds based on the liquid average velocity between 0.1 and 66. The liquid density was the same ( $1.0 \times 10^3 \text{ kg m}^{-3}$ ), which lead to Sc values of  $7.5 \times 10^3$ ,  $3.7 \times 10^4$  and  $4.6 \times 10^4$ . Benzoic acid was selected as the solid material since it is highly soluble in aqueous solutions and its physical properties are widely described [33].

Initially, wall-2 region was the only source of benzoic acid (called from now on as soluble wall) and the flowing liquid was free of solute. The length  $L$  of this soluble wall was  $2D$  in a total tube length of  $20D$ . The species transport equations were solved defining the liquid as solvent and benzoic acid as the solute with a molecular diffusion coefficient ( $D_m$ ) of  $1.0 \times 10^{-9} \text{ m}^2 \text{ s}^{-1}$ . In all the cases concerning single phase flow, the simulations were stopped when the benzoic acid distribution reached a stationary value throughout the entire domain.

### 2.2. Mass transfer simulations in the presence of the Taylor bubble

A second set of simulations was performed to study the role of the Taylor bubble flow in the mass transfer between the soluble wall and the flowing liquid. A bubble was added to each monophasic system (described in Section 2.1) when the concentration and velocity fields reached a stationary state inside the domain. The Reynolds number based on the bubble velocity varied between 0.1 and 100 (corresponding to the same values of the Reynolds number based on the average liquid velocity considered in Section 2.1) and the Capillary number ranged between 0.03 and 2.

The initial shape of the bubble was set as a quarter of a circle (the bubble nose) linked to a rectangle with a width equal to the radius of the circle (the bubble body). The bubble was initialized

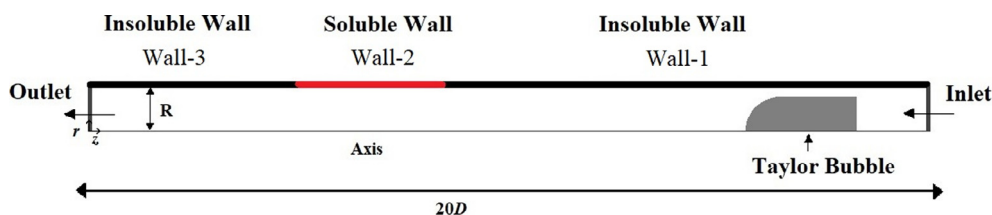


Fig. 2. Schematic representation of the domain and boundary conditions.



near the tube inlet in order to have the maximum available length of the domain to flow through. When the Taylor bubble reached the soluble wall region (wall-2), its shape was already definitive, and the flow was stabilized.

### 3. Results and discussion

#### 3.1. Mesh sensitivity tests

Based on the work previously done in similar domains, Rocha et al. [23] performed mesh density tests concerning solely the fluid flow. The authors used meshes ranging from 35,000 to 140,000 elements to guarantee that, in the radial direction, the film region comprised at least 5 cells. As such, it was necessary to perform some preliminary mesh independence tests to define an adequate grid density that ensures an accurate numerical description of the mass transfer phenomenon.

In order to reduce the computational effort, but still evaluate the density required for the mass transfer feature, the referred mesh tests were made with simpler scenarios of liquid phase-flow, i.e., in the absence of Taylor bubbles. For the range of densities tested, all the meshes were uniform and the information about the number of nodes in the axial ( $z$ ) and radial ( $r$ ) direction is given in Table 1.

In Fig. 3, radial concentration profiles obtained in three regions of the soluble wall are compared for different meshes. The profiles obtained with meshes MD and ME are practically coincident in those regions and, based on this observation, MD was the mesh density chosen to be used throughout this study.

#### 3.2. Validation of the mass transfer for monophasic systems

As the liquid flows through the soluble wall, a mass boundary layer tends to develop and, assuming constant hydrodynamic conditions, will eventually reach a stationary state.

With this concept in mind, local mass transfer coefficients ( $k$ ) can be determined along the soluble wall from the corresponding simulation results:

$$k = \frac{D_m}{c^* - c_{bulk}} \left. \frac{dc}{dr} \right|_{r=R} \quad (13)$$

where  $D_m$  stands for the diffusion coefficient,  $c^*$  is the solubility concentration and  $c_{bulk}$ , the bulk concentration.

The estimation of the average mass transfer coefficients ( $\bar{k}$ ) can be made from the integration along the soluble wall of the referred local coefficient values:

$$\bar{k} = \frac{1}{L} \int_{z_0}^{z_z} k dz \quad (14)$$

where  $L$  is the length of the soluble wall.

In order to assess the accuracy of the mass transfer numerical data produced for monophasic systems, the values determined for the mass transfer coefficients were compared with those predicted with available theoretical information. For that purpose, Equation (15) was found in the literature [34] and allows to predict

mass transfer coefficients in systems with monophasic flow inside macro-tubes.

$$Sh = 1.077 Re^{1/3} Sc^{1/3} \left( \frac{D}{L} \right)^{1/3} \quad (15)$$

It is important to notice that, this correlation was developed assuming short contact times and laminar monophasic flows, so, it can also be used to roughly estimate the wall-liquid Sherwood number in micro-scales.

The data for monophasic systems can also be compared to the expression reported by Shah and London [35], and used by van Baten and Krishna [30], assuming that  $\varepsilon_G$  for monophasic systems is 0.

$$Sh = 1.62 \frac{L_{tube}(1 - \varepsilon_G) D_m^{-1/3}}{D^2 u_b} \quad (16)$$

The Sherwood values determined from the data of the single-phase flow simulations and the ones estimated by Eqs. (15) and (16) are shown in Table 2. Although the Reynolds number varied by two orders of magnitude, the agreement between the numerical and correlations predictions of  $Sh$  is within a satisfactory margin (<26% for Eq. (15) and <48% for Eq. (16)).

#### 3.3. Taylor bubble influence on wall-liquid mass transfer

In order to make a comprehensive mass transfer study, as already mentioned, the work developed by Rocha and coworkers [23] was used as reference to set the different hydrodynamic behaviors involved on Taylor bubble flow in milli/micro-channels: case A (no recirculation), case B (closed wake following the bubble) and case C (recirculation areas ahead and below the bubble). Different parameters are compared for the different cases in order to predict the effect of the bubble presence on the mass transfer.

##### 3.3.1. Characteristics

Regarding the simulation of a system characterized by the first type of the aforementioned flow behaviors, the bubble Reynolds number was set to 10 ( $Re_B = 10$ ) while the Capillary number was 2 ( $Ca_B = 2.0$ ). According to Fig. 4, in a MRF, it was confirmed the absence of regions with liquid in recirculation. The bubble nose is lean and the tail presents a concave shape. A liquid film with a thickness of  $0.16D$  ( $\pm 0.2\%$ ) was detected between the bubble and the wall. It was estimated that the presence of the bubble affected the liquid flow above its nose only within a small length ( $Z'/D = 0.3$ ). Below the bubble, the liquid velocity profile is fully restored also after a short distance ( $L_{min}/D = 0.6$ ).

To analyze the second flow behavior previously mentioned (case B), the bubble Reynolds number was set to 100 ( $Re_B = 100$ ) and the Capillary number to 0.8 ( $Ca_B = 0.8$ ). Based on the corresponding simulation results, the bubble has a slender shape and, at the bubble rear, there is liquid in closed recirculation (MRF) flowing upwards attached to the bubble (Fig. 4). A liquid film between the bubble and the wall with a thickness of  $0.13D$  ( $\pm 5\%$ ) is also present. Behind the bubble, the undisturbed velocity profile in the liquid is restored after a much longer distance when compared with case A.

Finally, focusing on case C, a simulation was performed for a bubble Reynolds number of 0.1 ( $Re_B = 0.1$ ) and a Capillary number of 0.03 ( $Ca_B = 0.03$ ). The bubble had a length of  $2.9D$  and moved at a velocity of  $0.046 \text{ m s}^{-1}$ . Its shape was characterized by a round nose and tail, and a very narrow liquid film separating its lateral surface from the wall. This liquid film had a thickness of about  $0.05D$  ( $\pm 5\%$ ). There were also identified semi-infinite recirculation

**Table 1**  
Number of nodes used in the meshes considered for the density test.

	Nodes in $r$	Nodes in $z$
MA	50	2000
MB	90	3600
MC	150	6000
MD	200	8000
ME	220	8800

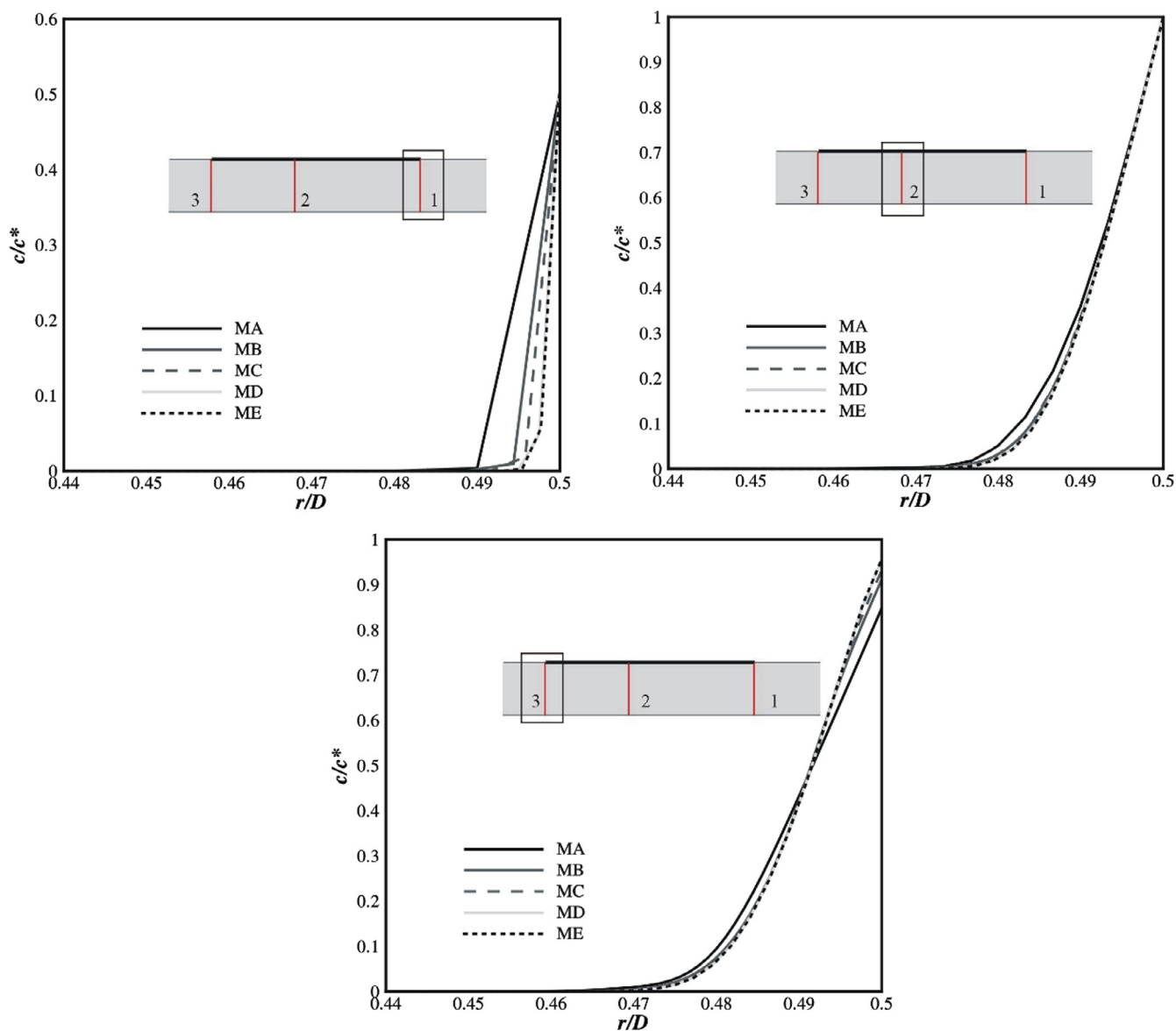


Fig. 3. Radial dimensionless concentration profiles for three positions along the soluble wall obtained for the different meshes considered in the density test.

Table 2

Sherwood numbers determined from the simulations of monophasic systems and corresponding values estimated by Eqs. (15) and (16).

	$Ca_B$	$Re_B$	$Sc$	$Sh_{sim}$	$Sh_{15}$	$Sh_{16}$
Case A	2	10	37,420	54.7	59.2	42.4
Case B	0.8	100	7483	61.7	77.5	54.8
Case C	0.03	0.1	45,800	19.0	16.7	9.9

zones (MRF) above and below the bubble which are evident from the streamlines representation.

### 3.3.2. Velocity profiles and wall shear stress

**3.3.2.1. Case A.** The variation of the wall shear stress along the soluble wall in a sequence of instants during the bubble passage is represented in Fig. 5(1) for case A. The radial profiles of the axial velocity component near the soluble wall are also represented for three different locations (A, B and C) along the bubble (Fig. 5(2)).

According to Fig. 5(2), as we move downwards along the bubble, the liquid flow velocity decreases strongly. In fact, in the

developed film region (location C) the liquid is almost stagnant. This decrease in velocity is accompanied by a decrease in the wall shear stress (Fig. 5(1)). This highly pronounced velocity reduction has an adverse effect on the process of wall-liquid mass transfer, as the reduced shear stresses do not favor the cleaning of the wall channels.

**3.3.2.2. Case B.** The wall shear stress for different instants and the radial profiles of the axial velocity component (close to the wall and for four different axial positions – A, B, C and D) are represented, for case B, in Fig. 6.

The flow pattern around the bubble is similar to what was obtained in case A. The liquid velocity decreases strongly along the developing liquid film region and, when it reaches a fully developed state (region D), it becomes almost stagnant. A very important effect of this velocity decrease is the lowering of the wall shear stress values (Fig. 6(1)). The only exception occurs in the wall enclosing the bubble nose, where there seems to be a slight increase in the wall shear stress due to higher values of the axial liquid velocity (region A). This kind of behavior becomes more evident in case C.

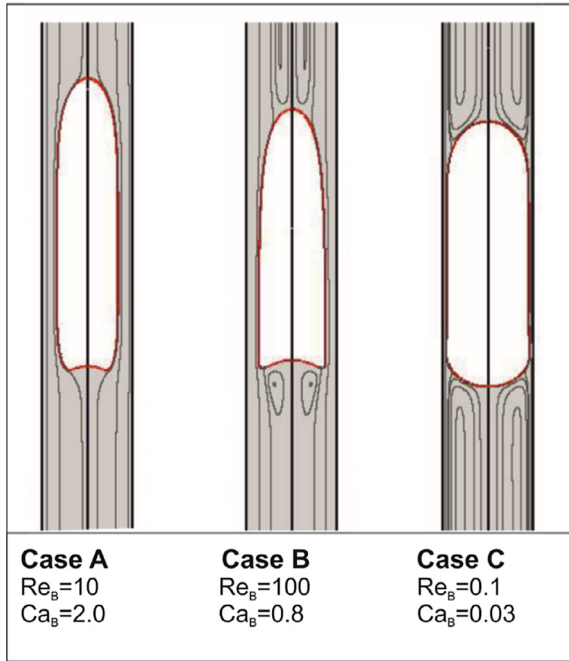


Fig. 4. Streamlines around the bubble in MRF representative of cases A, B and C.

3.3.2.3. *Case C.* The behavior of the wall shear stress along the soluble region was assessed at four different instants of the bubble passage for case C. The corresponding results are presented in Fig. 7, together with the radial profiles (in the vicinity of the wall) of the axial velocity component at three different positions (Fig. 7(2)).

According to the right side of Fig. 7, the magnitude of the liquid velocity in single phase flow is very low. In the presence of the Taylor bubble, the velocity in the liquid film is even lower and it

becomes stagnant when it reaches a fully developed state. This stagnancy on the liquid film corresponds to a wall shear stress around zero, but this hydrodynamic feature increases considerably around the nose and the tail of the bubble. According to the results on Fig. 7(1), it reaches values three times higher than those characteristic of a liquid single-phase flow. This enhancement of the wall shear stress values can have a highly positive effect on the cleaning of wall channels.

### 3.3.3. Axial and radial dispersion

As already shown, the bubble affects the velocity field in its surroundings, and so, it is expected that its presence will also influence the mass dispersion inside the tube. In order to better understand the bubble passage influence on the mass dispersed along the tube, different regions were defined according to the soluble wall position and to the direction of the co-current flowing liquid: a pre-soluble, a soluble and a post-soluble region.

3.3.3.1. *Case A.* In Fig. 8, axial concentration profiles taken in a radial position near the wall ( $r_i = 0.98D$ ) are presented for case A. Each profile concerns a different moment according to the bubble position within the domain, e.g., N 3.6D means that the bubble nose is 3.6D ahead of the beginning of the soluble wall. The soluble wall is located between  $0 < (z_w - z)/D < 2$ .

According to these results, the bubble passage is responsible for a slight increase in the solute concentration in the liquid enclosed between the bubble and the soluble wall ( $0 < (z_w - z)/D < 2$ ). Ahead of this section of the wall, in the post-soluble region, there is a small cleaning effect, i.e., the concentration decreases when compared with a liquid-phase flow. In the pre-soluble region there is also a slight alteration in the concentration field (Fig. 8A), i.e., there is some solute dragged into this region especially when the bubble is in the zone delimited by the soluble wall.

Fig. 9 shows radial concentration profiles at the middle of the soluble wall for different moments of the bubble passage – case

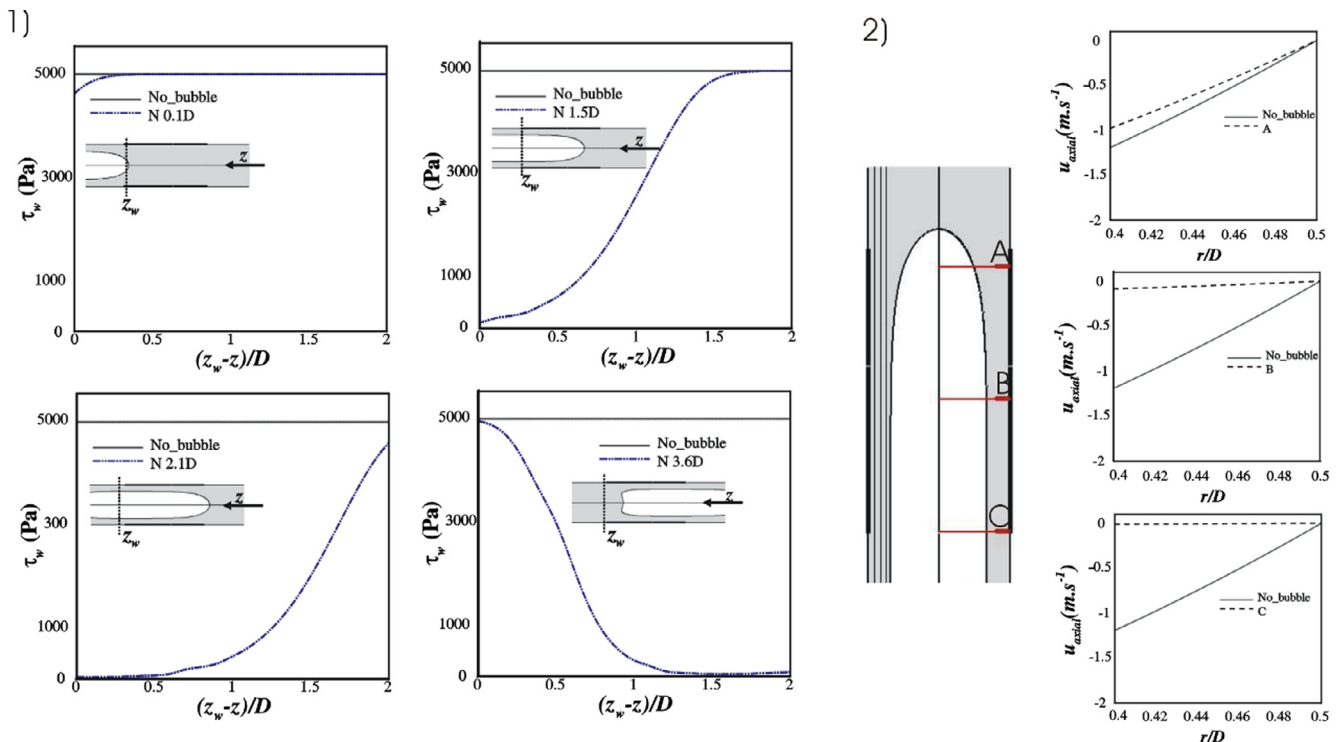
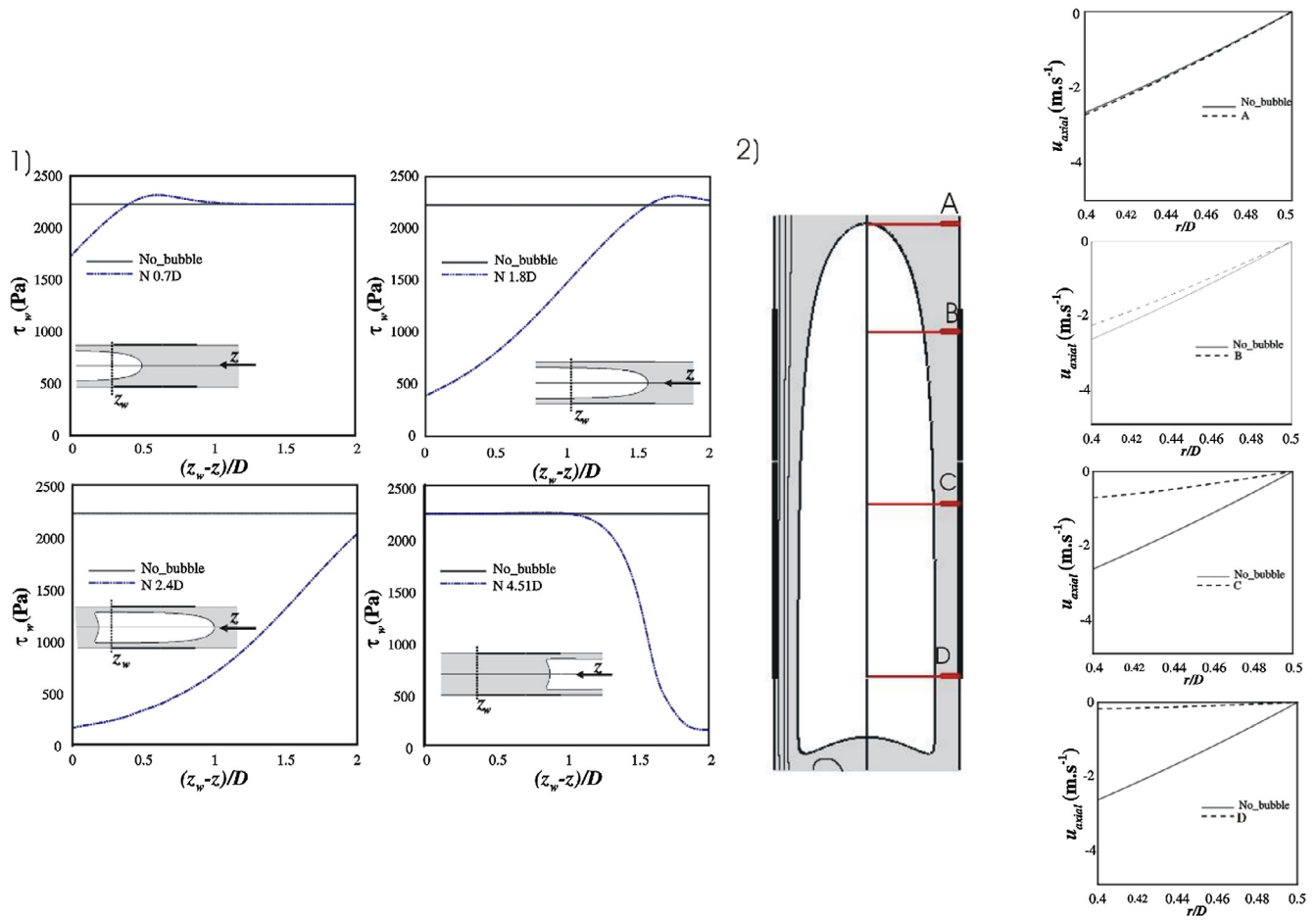
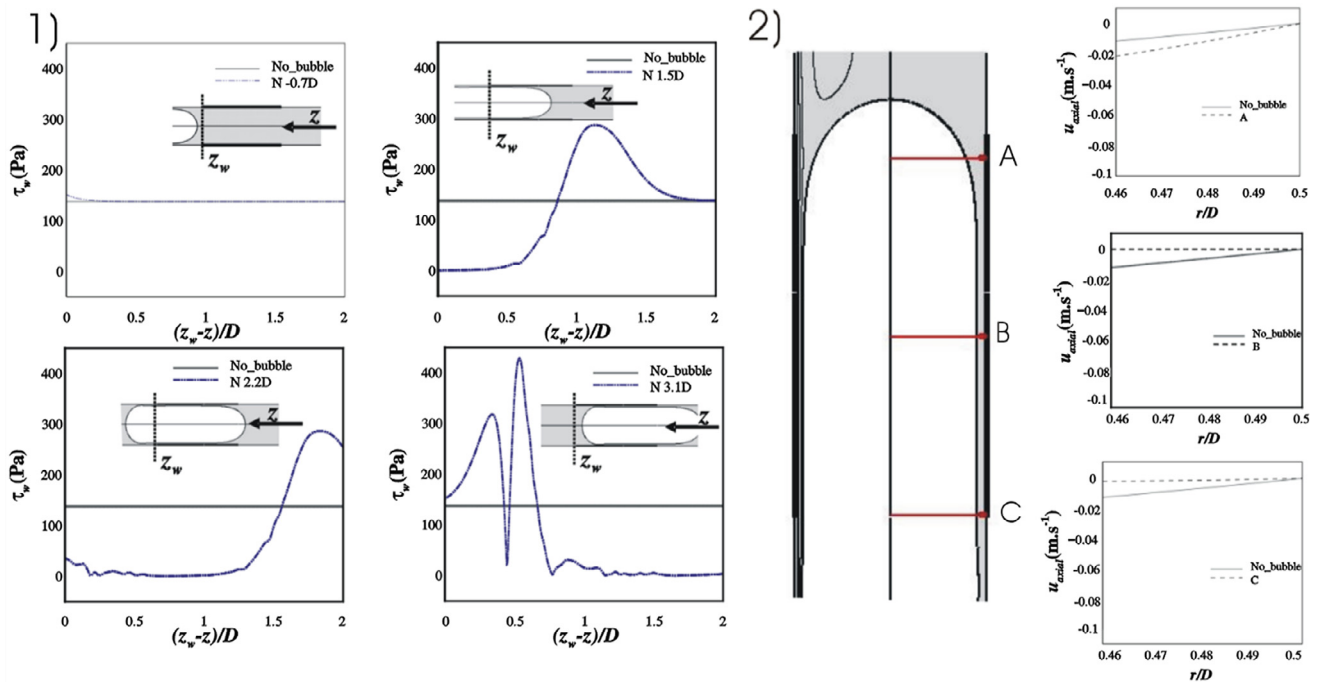


Fig. 5. (1) Wall shear stress along the soluble wall for different instants during the bubble passage; (2) radial profiles of the axial velocity component for three locations (A, B, C) along the Taylor bubble. A set of streamlines near the wall are represented on the left side of the bubble – case A.



**Fig. 6.** (1) Wall shear stress along the soluble wall for different instants during the bubble passage; (2) radial profiles of the axial velocity component for four locations (A, B, C, D) along the Taylor bubble. The streamlines near wall are represented on the left side of the bubble – case B.



**Fig. 7.** (1) Wall shear stress along the soluble wall for different instants during the bubble passage; (2) radial profiles of the axial velocity component for three locations (A, B, C) along the Taylor bubble – case C.



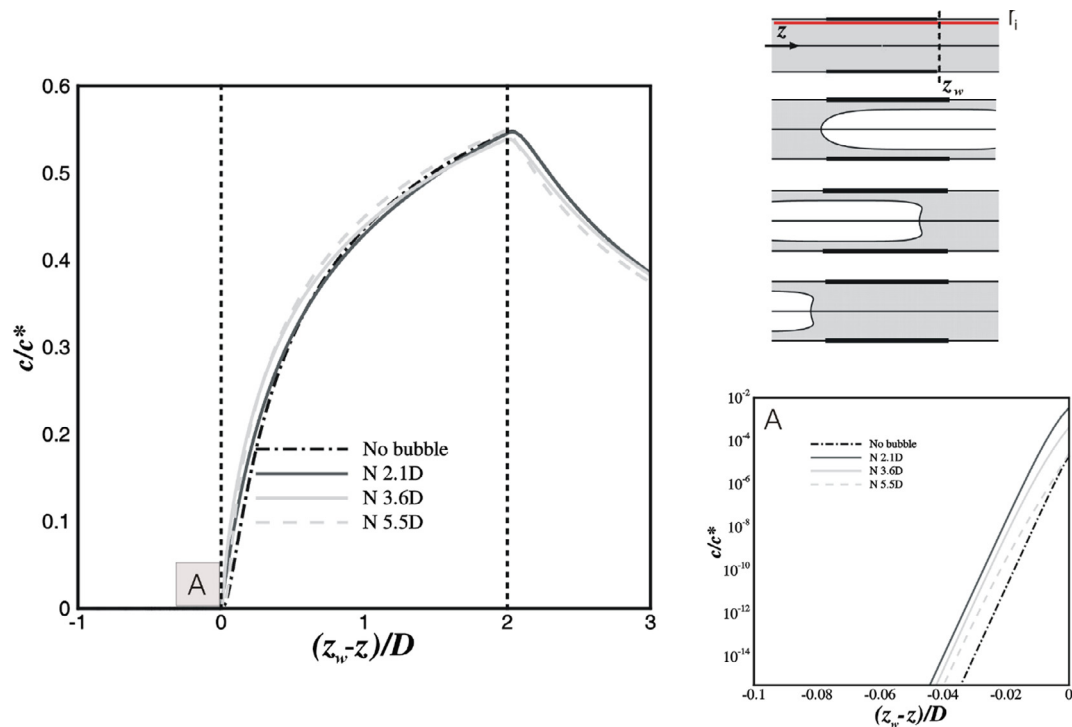


**Fig. 8.** Numerical axial normalized concentration profiles for a radial position near the wall (line in red in the sketch at the right side of the plot ( $r_i = 0.98D$ )). A schematic representation of the bubble position for each profile is also presented (top right). Plot A is a zoom in the pre-soluble wall region to better visualize the results (bottom right) – case A.

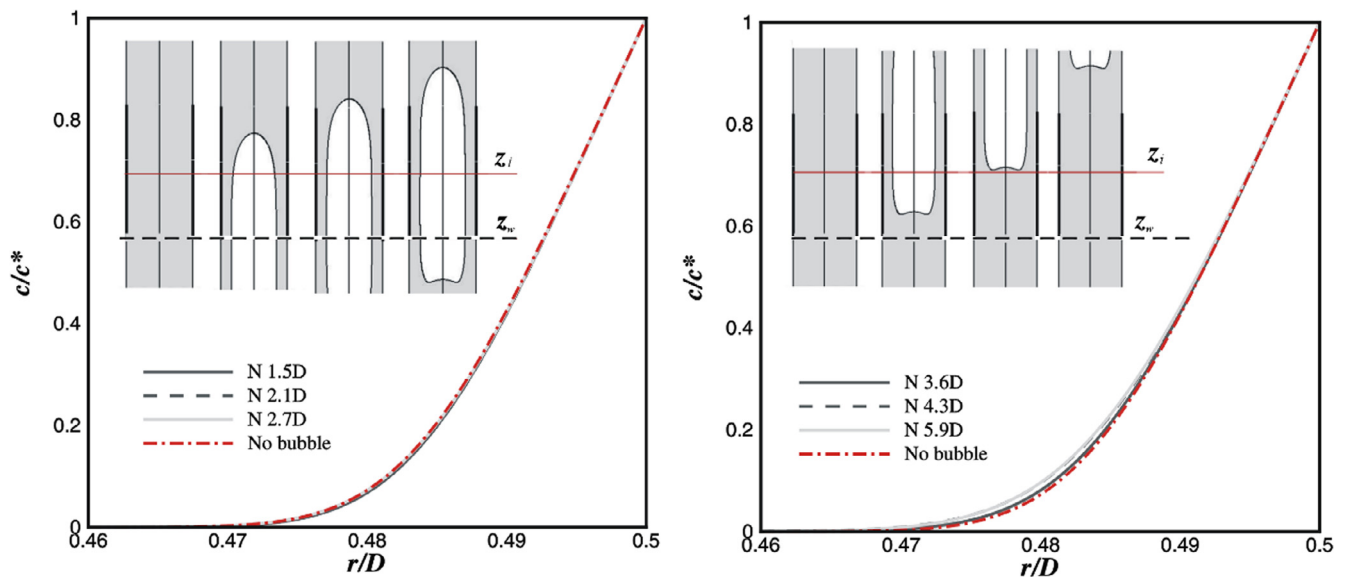


**Fig. 9.** Numerical radial normalized concentration profiles at the middle of the soluble wall for different instants of the bubble passage. A schematic representation to visualize the different bubble positions is also given –  $z_w$  sets the beginning of the soluble wall and  $z_i$  is the middle position under consideration in this figure – case A.

A. Until the position of the bubble nose is above  $1.5D$  from the beginning of the soluble wall, the slope of the concentration profiles remains constant. As the bubble moves further away from the soluble region, the concentration values increase slightly in radial positions more distant from the wall.

The main conclusion taken from Figs. 8 and 9 is that, for case A, the bubble passage is responsible for a slight increase on the axial and radial solute dispersion. The axial dispersion occurs in the backward direction and it is more evident in the post-soluble and soluble regions. Regarding the radial dispersion, this feature

is more visible after the bubble passage and is responsible for an increase of concentration in inwards regions.

**3.3.3.2. Case B.** As seen in case A, the axial concentration profiles acquired for case B (Fig. 10) show that the bubble movement induces a backward mass dispersion. The bubble passage reduces the quantity of mass ahead the soluble wall and promotes a slight increase of mass in the region enclosed by the soluble wall. Once again, there is a small quantity of solute dragged into the pre-soluble region (Fig. 10A).

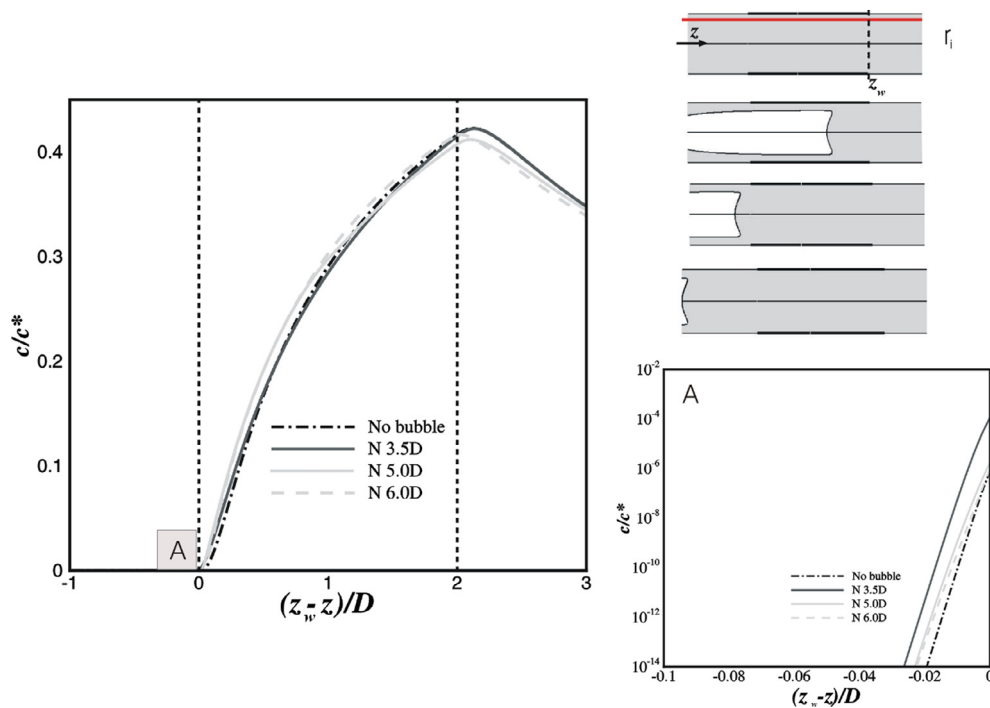


**Fig. 10.** Numerical axial dimensionless concentration profiles for a radial position near the wall (red line in the sketch at the right side of the plot ( $r_i = 0.98D$ )). A schematic representation of the bubble position for each profile is also presented. Plot A is a zoom performed on the pre-soluble region of the wall – for case B.

To visualize possible radial dispersion effects for case B, a set of radial concentration profiles taken on the middle of the soluble wall are plotted for different instants of the bubble passage. Until the closed wake that flows behind the bubble completely enters the soluble wall region, there is no detectable change on the radial concentration profiles (left side of Fig. 11). During the passage of this wake through the soluble wall, it becomes visible a slight radial dispersion (line N 4.5D), for an inner region.

**3.3.3.3. Case C.** In order to detect the mass dispersion caused by the bubble flow for case C, the dimensionless concentration fields in the vicinity of the soluble wall are represented in Fig. 12 for a sequence of instants. To make this detection possible, it was necessary that the mass boundary layer established before the bubble passage had enough thickness to reach into the liquid in recirculation

(see streamlines in plot 1 of Fig. 12). This can be particularly visible at the end of the soluble wall. When the bubble nose reaches this liquid region, there is a clear radial dispersion that can be observed in plots 4–5. In the bubble tail, a radial dispersion behavior is also present, which is caused by the expansion of the liquid coming from the film. The concavity of the tail of the bubble favors this dispersion (plots 6–8).

For a more detailed analysis of the mass dispersion, axial (Fig. 13) and radial (Fig. 14) dimensionless concentration profiles are plotted for different moments of the bubble passage past the soluble wall.

According to the results on Fig. 13, during the moments (N 2.6D; N 3.0D) the bubble is enclosed by the soluble wall, the concentration values along the boundary layer are lower than those obtained when the bubble is absent. When the bubble leaves the

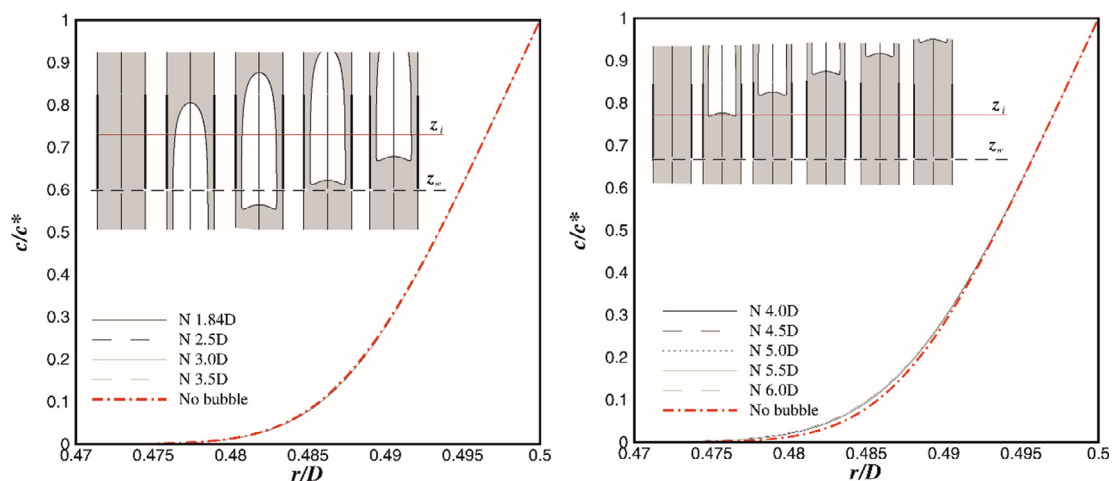


**Fig. 11.** Numerical radial dimensionless concentration profiles on the middle of the soluble wall taken at different instants of the bubble passage. The schematic representation of the bubble position is also presented – the soluble plate beginning ( $z_w$ ) and the considered position ( $z_i$ ) are marked – for case B.

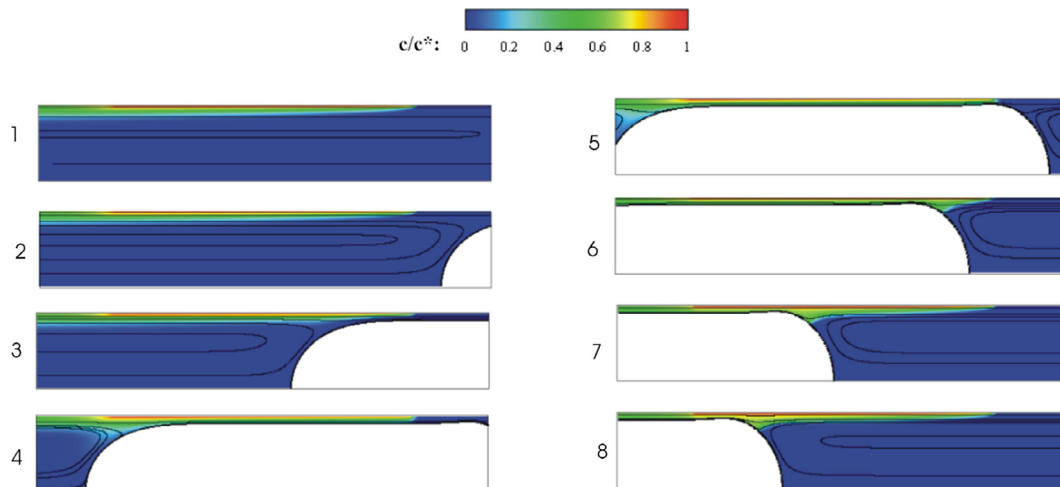


Fig. 12. Dimensionless concentration contours for different instants during the bubble passage in the soluble wall region.

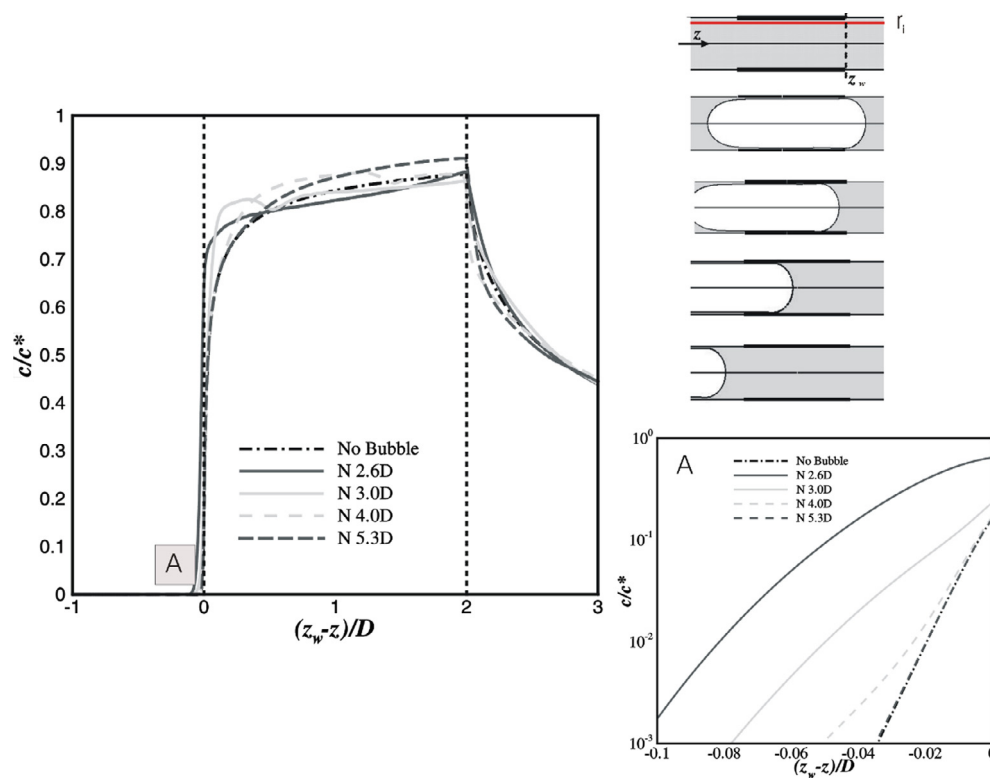


Fig. 13. Numerical axial dimensionless concentration profiles for a radial position near the wall (red line in the sketch of the right side of the plot ( $r_1 = 0.98D$ )). A schematic representation of bubble position for each profile is also presented. Plot A is a zoom performed on the pre-soluble region of the wall – for case C.

soluble region (N 5.3D), the solute concentration suffers an increase and becomes definitively higher in comparison with a single-phase flow scenario. Special attention should be given to lines N 3.0D and N 4.0D due to the presence of some oscillations. These oscillations are justified by the solute dispersion near the bubble nose and tail as explained on the discussion of Fig. 12. The same behavior happens in the post-soluble zone.

It is important to notice that, in this scenario (case C), it is possible to detect the presence of solute in the pre-soluble wall zone, even prior to the bubble entering the soluble region. This mass appears due to a backwards diffusion phenomenon that becomes evident due to the low levels of liquid velocity reported in Fig. 7. The concentration near the soluble wall inception increases on a

first moment when the bubble occupies all the soluble wall and it decreases as the bubble exits the soluble zone.

Regarding radial dispersion, during the bubble passage the radial concentration profiles show a magnitude decrease (left side of Fig. 14). After the bubble passage through the soluble region, there is a momentarily increase followed by a decrease (right side of Fig. 14). As it was previously mentioned about Fig. 12, the effect of solute dispersion near the bubble tail is responsible for this behavior.

### 3.3.4. Mass transfer coefficients

3.3.4.1. Case A. At this point, and based on the simulation data obtained for case A, the average mass transfer coefficients on the

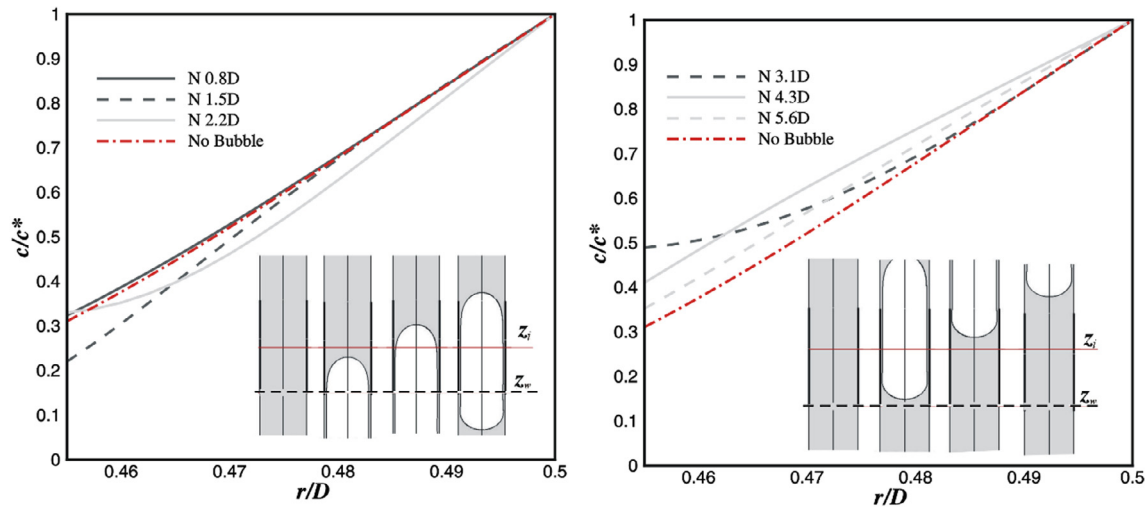


**Fig. 14.** Numerical radial dimensionless concentration profiles on the middle of the soluble wall for a sequence of moments during the bubble passage. The schematic representation of the bubble position is also presented – the soluble plate beginning ( $z_w$ ) and the considered position ( $z_i$ ) are marked – for case C.

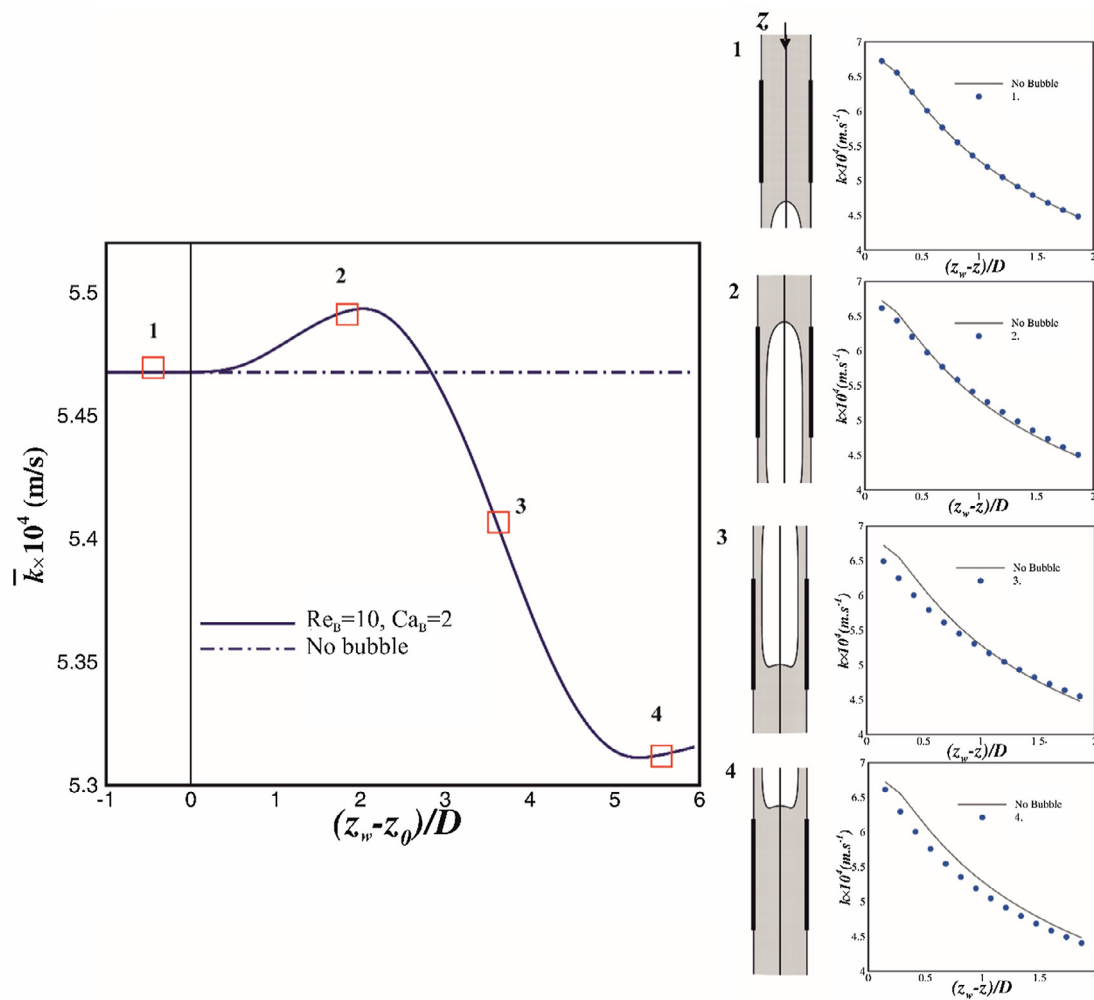


**Fig. 15.** Average mass transfer coefficients along the soluble wall during the bubble passage (left side). The coordinate  $(z_w - z_0)/D$  represents the distance of the bubble nose from the starting point of the soluble wall. Local mass transfer coefficients as a function of the distance to the beginning of the soluble plate,  $(z_w - z)/D$ , (right side). The average coefficients for these specific moments are marked by red boxes placed along the curve of the left side plot – case A.

soluble wall were estimated. In the left plot of Fig. 15, the values of this parameter are represented as a function of the bubble position during its passage through the soluble wall.

The bubble presence increases the average mass transfer coefficient until a maximum value is reached approximately when its nose is about to leave the soluble area. After that, the mass transfer coefficient decreases and falls to values lower than that observed in the bubble absence. The coefficients decrease starts after the bubble passage near the inception of the soluble section (third bubble position marked on the local mass-transfer coefficients in the right side of Fig. 15) and maintains as the bubble leaves the soluble wall (see fourth bubble position).

The concentration fields in the vicinity of the ending of the soluble wall are represented in Fig. 16 (top) for three different instants of the bubble passage through the soluble region. In order to facilitate the interpretation of this scheme, the values of the liquid thickness where the solute concentration is higher than 10% of  $c^*$  are also shown. Focusing now in the inception zone of the soluble wall, the concentration contours for different instants after the bubble passage are also represented in Fig. 16 (bottom).

From the results of Fig. 16 (top), it was detected a slight thinning behavior of the mass boundary layer caused by the liquid flow that comes from the post-soluble zone. This behavior is responsible for the increase of the average mass transfer coefficient that was observed in Fig. 15 (second moment). A similar study performed in conventional scale tubes [11], reported a more pronounced presence of this kind of cleaning effect on the mass boundary layer.

It is also possible to see that the bubble passage induces a backward mass dispersion near the inception of the soluble wall (bottom of Fig. 16). In agreement with the conclusions taken for macro-scales [11], this dispersion is responsible for the decrease of the average mass transfer coefficient as it was observed in Fig. 15 (third and fourth moments).

**3.3.4.2. Case B.** Similarly to what was done for case A, the mass transfer coefficients at different axial locations within the soluble wall and different instants of the bubble passage were numerically predicted. From these values, average coefficients were estimated and are represented in Fig. 17 (left side). These coefficients corroborate the conclusions drawn from the concentration profiles plots and are in line with those from case A: the average mass transfer

coefficient increases until a maximum value is reached (approximately when the nose is exiting the soluble region); after that, the mass transfer coefficient decreases and falls to values below the one observed in the bubble absence. This decrease starts when the bubble passes the inception of the soluble region and extends throughout its path along the soluble wall (see local mass-transfer coefficients in the right side of Fig. 17).

**3.3.4.3. Case C.** As with the other two scenarios, the average and local mass transfer coefficients obtained for case C are represented in Fig. 18.

The average mass transfer coefficient reaches its maximum value when the bubble nose is more or less at the middle of the region enclosed by the soluble wall. As it can be seen on the right side of Fig. 18, the bubble nose presence increases the local coefficients which justify the increase in the global mass transfer coefficient for this instant. As the bubble moves through the soluble wall, the coefficients start to decrease. However, a slight jump on these values is predicted when the bubble tail passes the soluble plate. This occurs because the tail region promotes a slight increase in the local mass transfer coefficients probably due to the sudden increase of the liquid velocity.

**3.3.4.4. Nose, film and tail effects.** To evaluate the effect of the bubble passage, the average mass transfer coefficients of each hydrodynamic region surrounding the bubble – nose, film and wake (Table 3) – were analyzed. The calculation of these average coefficients was based on the local mass transfer coefficients at different axial positions and different instants. The mass transfer coefficients for liquid only flow were also numerically acquired and their values are used as reference under the designation of  $k_{mp}$ .

Comparing with the results for single phase flow and regarding case A, at the nose and film there is a small increase of the mass transfer coefficients values. In the tail (lower region of the bubble where the bubble shape starts to get round), the coefficient shows a slight decrease when compared with monophasic flow. The referred increase in the coefficient values (nose and film) is explained by the change on the velocity field near the wall due to the presence of the bubble and by the renewal of the mass boundary layer due to the liquid movement.

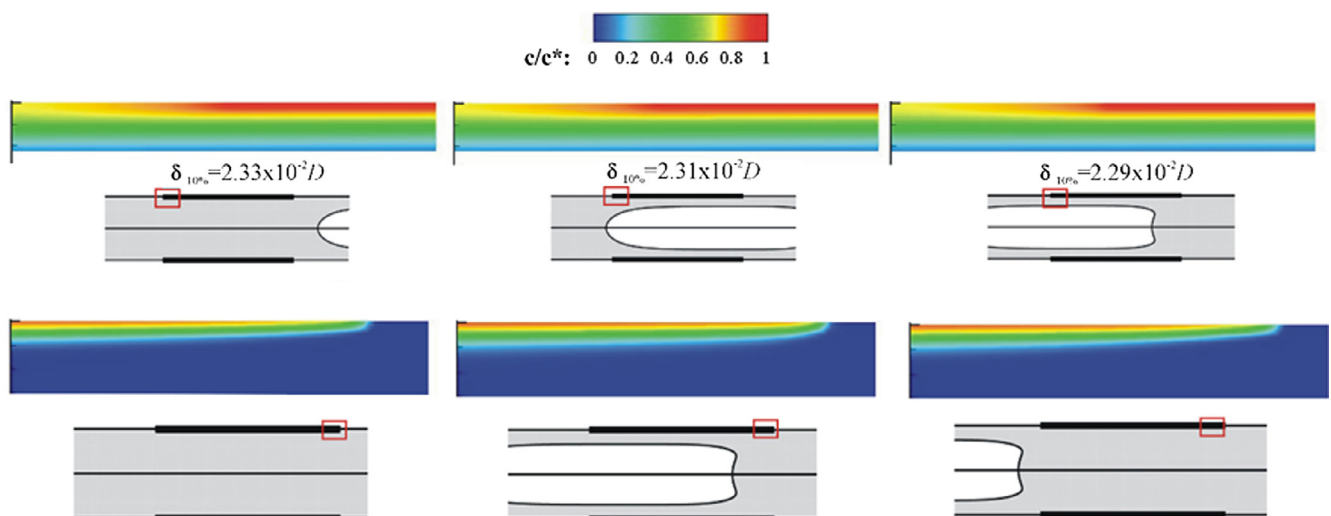


**Fig. 16.** On top, dimensionless concentration contours at the end of the soluble wall obtained for case A ( $Re_B = 10$  and  $Ca_B = 1$ ). Results are shown for three instants of the bubble passage. The thickness value of the boundary layer that corresponds to 10% of the solubility is also presented ( $\delta_{10\%}$ ). At the bottom of the figure, dimensionless concentration contours at the inception of the soluble wall are shown for the same case. Results are, once again, for three instants: before, during and after the bubble passage.



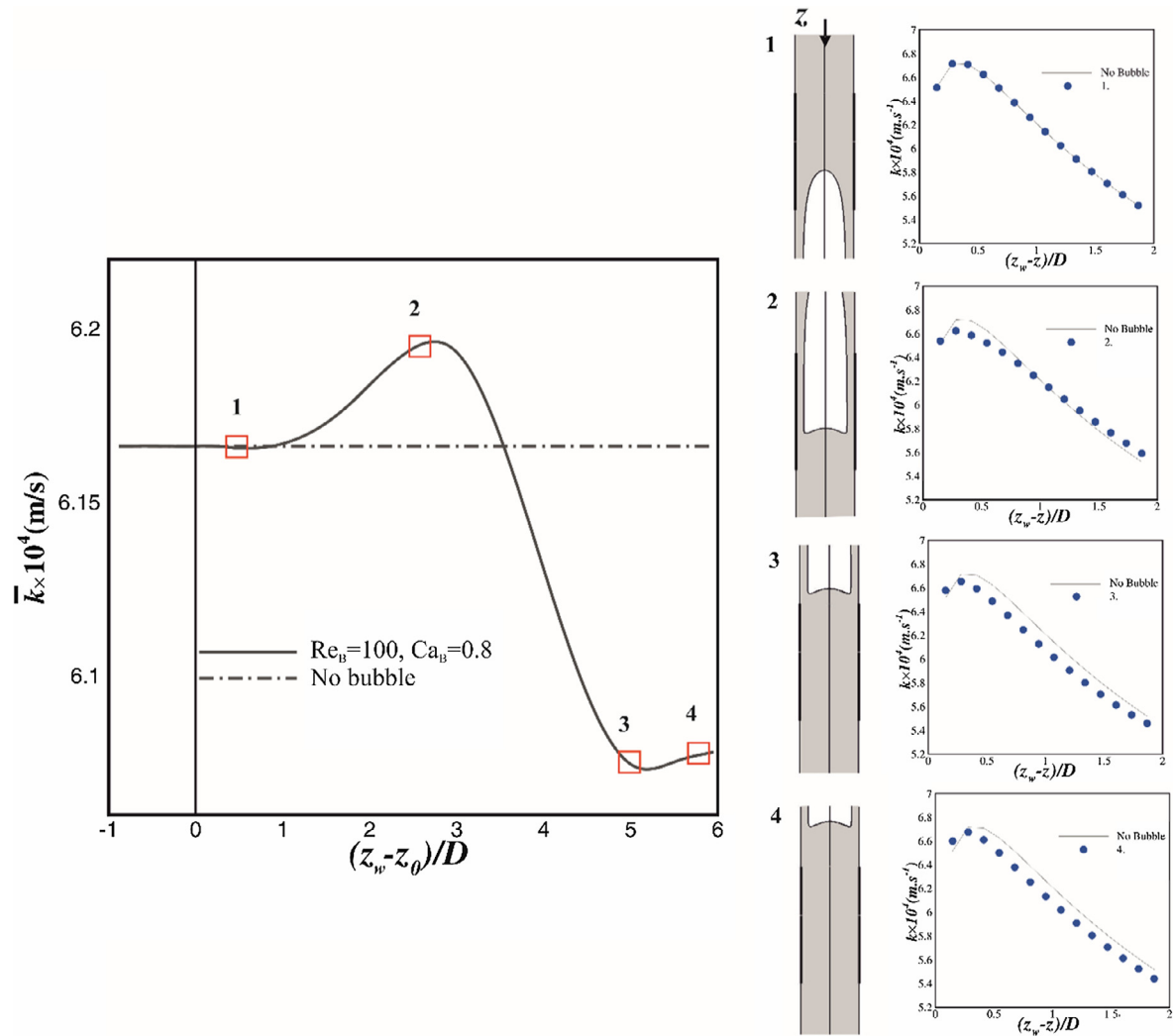


**Fig. 17.** Average mass transfer coefficients along the soluble wall (left side). The coordinate  $(z_w - z_0)/D$  represents the distance of the bubble nose to the starting of the soluble wall. Local mass transfer coefficients as a function of the distance to the beginning of the soluble plate,  $(z_w - z)/D$ , (right side). The average coefficients for these specific moments are marked by red boxes placed along the curve of the left side plot – case B.

Despite the presence of a closed wake flowing attached to the bottom of the bubble, the behavior of the average mass transfer coefficients in case B is very similar to case A. Once more, there is a small increase on the mass coefficients in the different bubble hydrodynamic regions when compared to the monophasic values. The tail appears as an exception that, as in case A, shows a decrease on the mass transfer coefficient value when compared with the single-phase flow.

In case C, the coefficient values reveal a clear difference compared with those for cases A and B: the mass transfer coefficient in the film is slightly lower than that obtained for single phase flow. This is an indication that, for this kind of flow behavior, the film does not enhance the mass transfer phenomenon. The stagnant liquid in the film during the bubble passage is responsible for this decrease. Furthermore, the decrease of the coefficient in the tail region is much more pronounced than in the other two scenarios.

**3.3.4.5. Comparison with data from literature.** For comparison purposes, in Table 4, the numerical Sherwood numbers computed from the average mass transfer coefficients are presented together with estimations made with correlations available in literature [28,29].

Regarding cases A and B, the numerical values show large deviations from the values calculated using the correlations. For case C, the Sh numerical predictions are of the same order of magnitude of those given by the correlations in the literature [28,29]. The fact that all these correlations are based on the stagnant film assumption justifies the better agreement with case C.

Besides the bubble/liquid plug characteristics, there is another important factor that may influence the values obtained from the correlations: the presence of more than one bubble in the system. Although there is no clear statement that the experimental studies cited used a bubble train, it is believed that the correlations described are not for isolate bubbles but for bubbles under the influence of others. This helps justify the difference between values from correlations and from numerical work.

### 3.4. Quantification of the bubble passage effect

As already mentioned, the tube was divided in three regions of similar area: a pre-soluble, a soluble and a post-soluble. In order to properly define the bubble passage effect on the mass transferred from the wall, this feature was quantified in the referred three regions for two different moments: before ( $m_{initial}$ ) and after ( $m_{final}$ ) the bubble passage through the soluble wall. Afterwards,

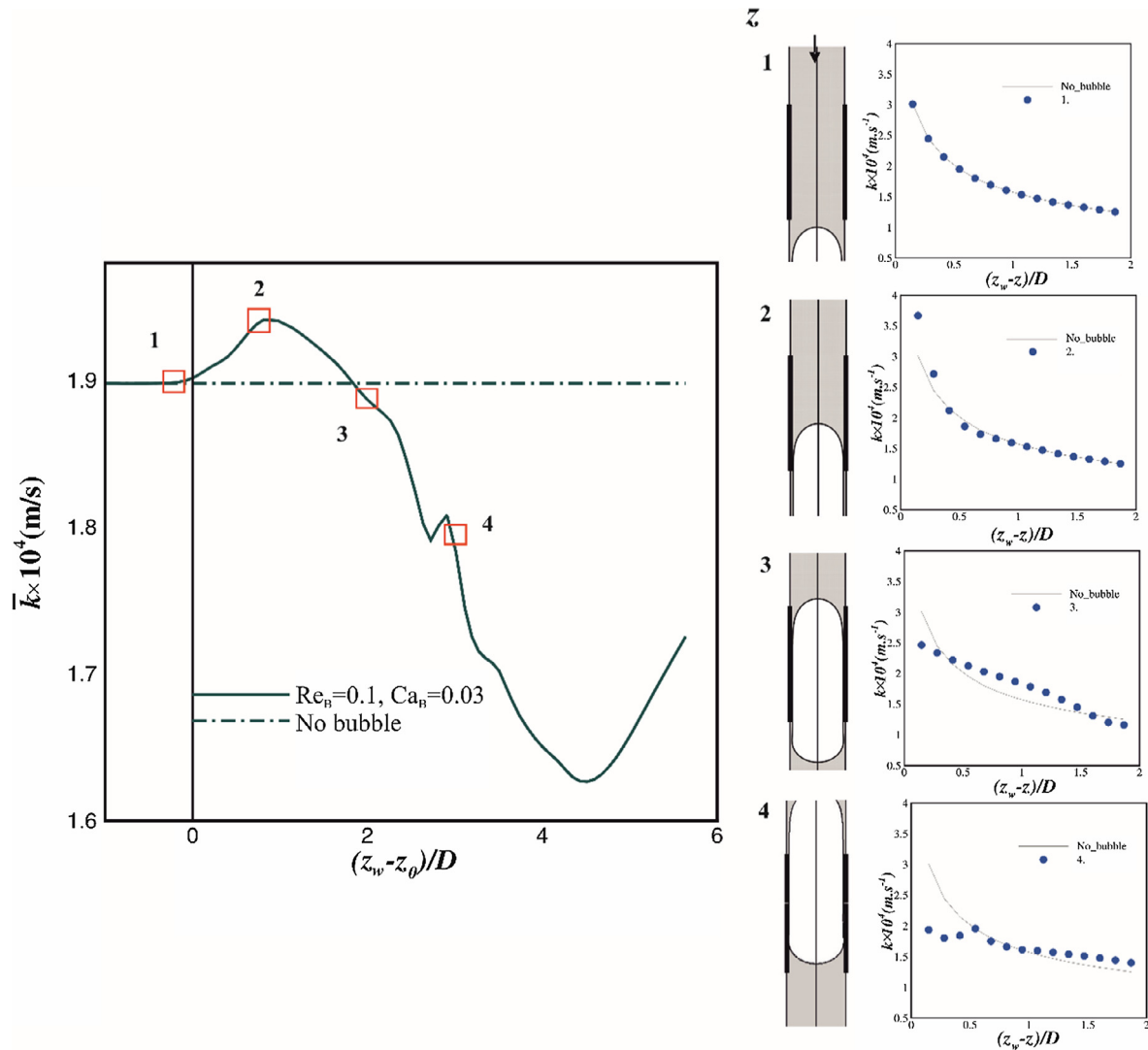


**Fig. 18.** Average mass transfer coefficients along the soluble wall. The coordinate  $(z_w - z_0)/D$  represents the distance of the bubble nose to the starting of the soluble wall. Local mass transfer coefficients as a function of the distance to the beginning of the soluble plate,  $(z_w - z)/D$ , (right side). The average coefficients for these specific moments are marked by red boxes placed along the curve of the left side plot – case C.

**Table 3**

Numerical average mass-transfer coefficients at the nose, film and tail regions. The corresponding deviations from the mass transfer coefficients for single phase flow ( $\bar{k}_{mp}$ ) are also presented.

	$\bar{k}_{mp} \times 10^4$	Nose		Film		Tail	
		$\bar{k}_n \times 10^4$	Dev (%)	$\bar{k}_f \times 10^4$	Dev (%)	$\bar{k}_t \times 10^4$	Dev (%)
Case A	5.47	5.51	0.82	5.64	3.07	5.40	−1.15
Case B	6.17	6.18	0.24	6.2	0.79	6.05	−1.86
Case C	1.95	2.01	3.25	1.95	−0.02	1.62	−16.87

**Table 4**

Sherwood numbers from correlations and from numerical data associated to the bubble passage.

	$Sh_{(eq. 6)}$	$Sh_{(eq. 7)}$	$Sh_{numerical}$
Case A	227	346	~55
Case B	326	125	~62
Case C	43	11	~19

**Table 5**

Variation of mass transferred in different zones, for cases A, B and C.

	Pre-soluble zone $\Delta m/m$ (%)	Soluble zone $\Delta m/m$ (%)	Post-soluble zone $\Delta m/m$ (%)	Total (%)
Case A	10.3	4.84	−1.19	1.84
Case B	3.64	3.21	−1.67	0.76
Case C	2.66	6.51	−16.8	−5.19

the mass variation ( $\Delta m/m$ ) was estimated and is presented in Table 5.

$$\Delta m/m = \frac{(m_{\text{final}} - m_{\text{initial}})}{m_{\text{initial}}} \times 100 \quad (17)$$

For each region the mass was solved by the integral:

$$m = \int_V \int c 2\pi r dr dz \quad (18)$$

In the pre-soluble region, no solute should be present before the bubble arrival, which is true for cases A and B. However, in case C, some solute is already present even before the bubble reaches the soluble wall. As previously explained, this particular feature is due to the diffusion effect that overcomes the convection when the liquid velocity is very low. For all three scenarios under consideration, the bubble passage increases the solute mass in the pre-soluble region. Case A is the one with the highest mass percentage increase and, inversely, case C has the lowest one. For the soluble region, the highest increase of mass regards case C, probably due the recirculation areas that end up throwing the solute on the soluble wall region. In the post soluble zone, all cases show a decrease of mass.

In terms of overall balance, case C leads to a reduction of mass on the system, while case A is the one that presents the highest increase.

#### 4. Conclusions

The growing attention over processes occurring in milli/micro-scales when compared with conventional sizes justifies a more fundamental research to deeply understand the phenomena on these small dimensions. Among these phenomena, the enhancement of the mass transfer is one of the most important, which would be crucial to help control biofilm formation on micro-devices.

In this work, the influence of slug flow pattern on wall-liquid mass transfer in micro-tubes was successfully studied using CFD techniques based on the VOF interface tracking method.

It was confirmed that the wall shear stress is highly affected by the presence of the Taylor bubble which may impact the mass transfer. In order to perceive the effect of the different hydrodynamic characteristics surrounding a Taylor bubble in a micro-tube, the mass transfer was studied numerically for three specific scenarios: in case A, the liquid presents no recirculation zones; in case B a closed wake follows the bubble; while in case C there are liquid recirculation zones above and below the bubble.

The first relevant conclusion is that bubble presence is responsible for an increase in radial and axial dispersions which is more visible in case C, where the liquid has recirculation zones ahead and below of the bubble.

Two types of mass transfer coefficients were considered in order to evaluate the effect of the bubble on the wall-liquid mass transfer: a global coefficient that evaluates the overall impact of the bubble and average coefficients that assess the effect on the different flow regions (nose, film and tail).

The presence of a single bubble leads to an increase of the global wall-liquid mass transfer coefficients for the cases under consideration. In the presence of more Taylor bubbles, this effect can be enhanced. The presence of a bubble-train flow (a sequence of bubbles separated by liquid slugs) is pointed as a way to improve the mass transfer face to monophasic fluids [36,37]. However due to the high complexity of the bubble-train flow, it is not easy to extrapolate or predict the effects on the mass transfer phenomena from the study of a single bubble. By introducing a new bubble on a system different effects can occur: for example, for case C the recirculation areas above and below the bubble will become closed,

while for case B, the presence of a closed wake can lead to coalescence among bubbles. A careful examination of the effect of a train bubble presence will be considered in future works.

Regarding the average coefficients in each flow region, for cases A and B, both nose and film regions promote an increase in these coefficients when compared with the values acquired for liquid monophasic systems, whereas the tail leads to an opposite behavior. In case C is verified an exception, i.e., only on the nose region was observed an enhancement of the mass transfer coefficients. The film region does not enhance the mass transfer phenomenon and that is probably due to the axial extent of stagnancy in the liquid.

Concerning the quantification of the mass transferred, the passage of a Taylor bubble promotes an increase of solute in the liquid for cases A and B. On the other hand, in case C, the bubble passage leads to a reduction of the solute available in the liquid phase.

Based on the numerical data produced, the main conclusion to extract from the present work is that the passage of a single Taylor bubble has a moderate positive effect on the wall-liquid mass transfer rate and solute distribution inside micro-tubes. This fact is a good indicator of the potential high impact that a train of bubbles may have in the referred phenomenon, and should be seen as the starting point to investigate more complex systems (with 2 or 3 consecutive bubbles). Furthermore, a more systematic study involving a wider range of cases should be considered in the future, in order to get a deeper understanding of the effect of different liquid velocities and bubble lengths on mass transfer.

#### Conflict of interest statement

None of the authors presently have or have had in the past any personal or financial relationships that may compromise the integrity of this work.

#### Acknowledgments

The authors acknowledge the support of FEDER funds through COMPETE2020—Operational Programme for Competitiveness Factors (POCI) and National Funds (PIDDAC) through FCT under projects PEst-OE/EME/UI0532 and POCI-01-0145-FEDER-031758. M. C.F. Silva also acknowledges the financial support provided by FCT through the PhD Grant PD/BD/52622/2014.

#### References

- [1] A. Gavrilidis, P. Angeli, E. Cao, K.K. Yeong, Y.S.S. Wan, Technology and applications of microengineered reactors, *Chem. Eng. Res. Des.* 80 (1) (2002) 3–30, <https://doi.org/10.1205/026387602753393196>.
- [2] P. Angeli, A. Gavrilidis, Hydrodynamics of Taylor flow in small channels: a review, *Proc. Instit. Mech. Eng. Part C J. Mech. Eng. Sci.* 222 (2008) 737–751, <https://doi.org/10.1243/09544062JMES776>.
- [3] M.T. Kreutzer, F. Kapteijn, J.A. Moulijn, J.J. Heiszwolf, Multiphase monolith reactors: chemical reaction engineering of segmented flow in microchannels, *Chem. Eng. Sci.* 60 (22) (2005) 5895–5916, <https://doi.org/10.1016/j.ces.2005.03.022>.
- [4] J.L. Xu, Y.H. Gan, D.C. Zhang, X.H. Li, Microscale heat transfer enhancement using thermal boundary layer redeveloping concept, *Int. J. Heat Mass Transf.* 48 (9) (2005) 1662–1674, <https://doi.org/10.1016/j.ijheatmasstransfer.2004.12.008>.
- [5] J. Yue, L. Luo, Y. Gonthier, G. Chen, Q. Yuan, An experimental study of air-water Taylor flow and mass transfer inside square microchannels, *Chem. Eng. Sci.* 64 (16) (2009) 3697–3708, <https://doi.org/10.1016/j.ces.2009.05.026>.
- [6] S. Corbel, N. Becheikh, T. Roques-Carnes, O. Zahraa, Mass transfer measurements and modeling in a microchannel photocatalytic reactor, *Chem. Eng. Res. Des.* 92 (4) (2014) 657–662, <https://doi.org/10.1016/j.cherd.2013.10.011>.
- [7] C. Kunin, Blockage of urinary catheters: Role of microorganisms and constituents of the urine on formation of encrustations, *J. Clin. Epidemiol.* 42 (9) (1989) 835–842, [https://doi.org/10.1016/0895-4356\(89\)90096-6](https://doi.org/10.1016/0895-4356(89)90096-6).
- [8] D.J. Stickler, J. King, J. Nettleton, C. Winters, The structure of urinary catheter encrusting bacterial biofilms, *Cells Mater.* 3 (3) (1993) 315–320.

- [9] P. Singha, J. Locklin, H. Handa, A review of the recent advances in antimicrobial coatings for urinary catheters, *Acta Biomater.* 50 (2017) 20–40, <https://doi.org/10.1016/j.actbio.2016.11.070>.
- [10] J. Zhang, W. Li, Investigation of hydrodynamic and heat transfer characteristics of gas–liquid Taylor flow in vertical capillaries, *Int. Commun. Heat Mass Transf.* 74 (2016) 1–10, <https://doi.org/10.1016/j.icheatmasstransfer.2016.03.003>.
- [11] M.C.F. Silva, J.D.P. Araújo, J.B.L.M. Campos, CFD studies coupling hydrodynamics and solid-liquid mass transfer in slug flow for matter removal from tube walls, *AIChE J.* 63 (6) (2017) 2420–2439, <https://doi.org/10.1002/aic.15610>.
- [12] J.W. Coleman, S. Garimella, Characterization of two-phase flow patterns in small diameter round and rectangular tubes, *Int. J. Heat Mass Transf.* 42 (15) (1999) 2869–2881, [https://doi.org/10.1016/S0017-9310\(98\)00362-7](https://doi.org/10.1016/S0017-9310(98)00362-7).
- [13] K.A. Triplett, S.M. Ghiaasiaan, S.I. Abdel-Khalik, D.L. Sadowski, Gas-liquid two-phase flow in microchannels Part I: two-phase flow patterns, *Int. J. Multiph. Flow* 25 (1999) 377–394, [https://doi.org/10.1016/S0301-9322\(98\)00054-8](https://doi.org/10.1016/S0301-9322(98)00054-8).
- [14] T.C. Thulasidas, M.A. Abraham, R.L. Cerro, Flow patterns in liquid slugs during bubble-train flow inside capillaries, *Chem. Eng. Sci.* 52 (17) (1997) 2947–2962, [https://doi.org/10.1016/S0009-2509\(97\)00114-0](https://doi.org/10.1016/S0009-2509(97)00114-0).
- [15] L. Chen, Y.S. Tian, T.G. Karayiannis, The effect of tube diameter on vertical two-phase flow regimes in small tubes, *Int. J. Heat Mass Transf.* 49 (21–22) (2006) 4220–4230, <https://doi.org/10.1016/j.ijheatmasstransfer.2006.03.025>.
- [16] H. Liu, C.O. Vandu, R. Krishna, Hydrodynamics of Taylor flow in vertical capillaries: Flow regimes, bubble rise velocity, liquid slug length, and pressure drop, *Ind. Eng. Chem. Res.* 44 (14) (2005) 4884–4897, <https://doi.org/10.1021/ie049307n>.
- [17] S. Nogueira, M.L. Riethmuller, J.B.L.M. Campos, A.M.F.R. Pinto, Flow patterns in the wake of a Taylor bubble rising through vertical columns of stagnant and flowing Newtonian liquids: An experimental study, *Chem. Eng. Sci.* 61 (22) (2006) 7199–7212, <https://doi.org/10.1016/j.ces.2006.08.002>.
- [18] S. Nogueira, M.L. Riethmuller, J.B.L.M. Campos, A.M.F.R. Pinto, Flow in the nose region and annular film around a Taylor bubble rising through vertical columns of stagnant and flowing Newtonian liquids, *Chem. Eng. Sci.* 61 (2) (2006) 845–857, <https://doi.org/10.1016/j.ces.2005.07.038>.
- [19] J. Fabre, A. Line, Modeling of two-phase slug flow, *Annu. Rev. Fluid Mech.* 24 (1) (1992) 21–46, <https://doi.org/10.1146/annurev.fl.24.010192.000321>.
- [20] J.D.P. Araújo, J.M. Miranda, A.M.F.R. Pinto, J.B.L.M. Campos, Wide-ranging survey on the laminar flow of individual Taylor bubbles rising through stagnant Newtonian liquids, *Int. J. Multiph. Flow* 43 (2012) 131–148, <https://doi.org/10.1016/j.ijmultiphaseflow.2012.03.007>.
- [21] T. Taha, Z.F. Cui, CFD modelling of slug flow in vertical tubes, *Chem. Eng. Sci.* 61 (2) (2006) 676–687, <https://doi.org/10.1016/j.ces.2005.07.022>.
- [22] P. Zaloha, J. Kristal, V. Jiricny, N. Völkel, C. Xuereb, J. Aubin, Characteristics of liquid slugs in gas-liquid Taylor flow in microchannels, *Chem. Eng. Sci.* 68 (1) (2012) 640–649, <https://doi.org/10.1016/j.ces.2011.10.036>.
- [23] L.A.M. Rocha, J.M. Miranda, J.B.L.M. Campos, Wide range simulation study of Taylor bubbles in circular milli and microchannels, *Micromachines*. 8 (5) (2017), <https://doi.org/10.3390/mi8050154>.
- [24] R. Gupta, D.F. Fletcher, B.S. Haynes, On the CFD modelling of Taylor flow in microchannels, *Chem. Eng. Sci.* 64 (12) (2009) 2941–2950, <https://doi.org/10.1016/j.ces.2009.03.018>.
- [25] F.P. Bretherton, The motion of long bubbles in tubes, *J. Fluid Mech.* 10 (02) (1961) 166, <https://doi.org/10.1017/S0022112061000160>.
- [26] N. Brauner, D.M. Maron, Identification of the range of “small diameters” conduits, regarding two-phase flow pattern transitions, *Int. Commun. Heat Mass Transf.* 19 (1) (1992) 29–39, [https://doi.org/10.1016/0735-1933\(92\)90061-L](https://doi.org/10.1016/0735-1933(92)90061-L).
- [27] R.E. Treybal, *Mass-Transfer Operations*, third ed., McGraw-Hill, Singapore, 1981.
- [28] V. Hatziantoniou, B. Andersson, Solid-liquid mass transfer in segmented gas-liquid flow through a capillary, *Ind. Eng. Chem. Fundam.* 21 (1982) 451–456, <https://doi.org/10.1021/i100008a024>.
- [29] G. Berčić, A. Pintar, The role of gas bubbles and liquid slug lengths on mass transport in the Taylor flow through capillaries, *Chem. Eng. Sci.* 52 (97) (1997) 3709–3719, [https://doi.org/10.1016/S0009-2509\(97\)00217-0](https://doi.org/10.1016/S0009-2509(97)00217-0).
- [30] J.M. van Baten, R. Krishna, CFD simulations of wall mass transfer for Taylor flow in circular capillaries, *Chem. Eng. Sci.* 60 (4) (2005) 1117–1126, <https://doi.org/10.1016/j.ces.2004.10.001>.
- [31] J.U. Brackbill, D.B. Kothe, C. Zemach, A continuum method for modeling surface tension, *J. Comput. Phys.* 100 (2) (1992) 335–354, [https://doi.org/10.1016/0021-9991\(92\)90240-Y](https://doi.org/10.1016/0021-9991(92)90240-Y).
- [32] J.D.P. Araújo, J.M. Miranda, J.B.L.M. Campos, Simulation of slug flow systems under laminar regime: Hydrodynamics with individual and a pair of consecutive Taylor bubbles, *J. Pet. Sci. Eng.* 111 (2013) 1–14, <https://doi.org/10.1016/j.petrol.2013.10.007>.
- [33] S. Irandoust, B. Andersson, Concentration-dependent diffusivity of benzoic acid in water and its influence on the liquid solid mass-transfer, *Can. J. Chem. Eng.* 64 (1986) 954–959, <https://doi.org/10.1002/cjce.5450640611>.
- [34] R.L. Fournier, *Basic Transport Phenomena in Biomedical Engineering*, 3rd ed., CRC Press, 2011, pp. 175–236.
- [35] R.K. Shah, A.L. London, *Laminar Flow Forced Convection in Ducts: A Source Book for Compact Heat Exchanger Analytical Data*, Academic Press, 1978, pp. 78–153.
- [36] C. Horvath, B.A. Solomon, J.-M., Engasser, Measurement of radial transport in slug flow using enzyme tubes, *Ind. Eng. Chem. Fundam.* 12 (4) (1973) 431–439, <https://doi.org/10.1021/i160048a006>.
- [37] R. Gruber, T. Melin, Radial mass-transfer enhancement in bubble-train flow, *Int. J. Heat Mass Transf.* 46 (15) (2003) 2799–2808, [https://doi.org/10.1016/S0017-9310\(03\)00053-X](https://doi.org/10.1016/S0017-9310(03)00053-X).